Rethinking Vibrational Stark Spectroscopy: Peak Shifts, Linewidths and the Role of Non-Stark Solvent Coupling

Sebastian M. Fica-Contreras, Aaron P. Charnay, Junkun Pan, Michael D. Fayer*
Department of Chemistry, Stanford University, Stanford, CA 94305
*phone: 650 723-4446; email: fayer@stanford.edu

Supporting Information

1. Density Functional Theory

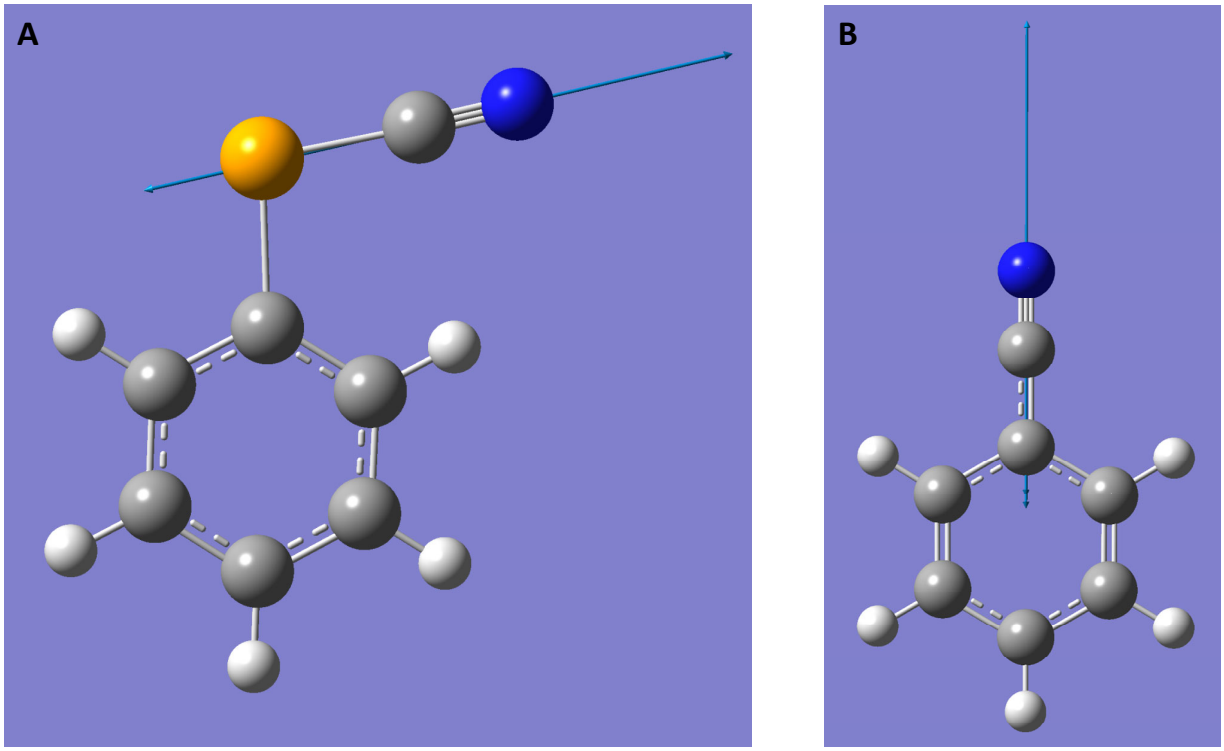

Figure S1. Optimized structures of PhSeCN and BZN calculated with Density Functional Theory. The functional used was B3WP91 and the basis set 6-311G (2df, p). A tight convergence criterion and a superfine integration grid were used. The arrows represent displacement vectors for the atoms involved in the CN stretching normal mode. Only two displacement vectors are observed in PhSeCN; one for each atom in the CN moiety. In BZN, three displacement vectors are observed: one for each atom in the CN moiety, and one for the *ipso* carbon on the phenyl ring. These observations indicate that in BZN, the CN stretching normal mode is not a local mode and that the phenyl ring is coupled to the CN vibration.

A vibrational frequency calculation was performed on the optimized structures and an anharmonic correction was performed on the CN stretching mode. A summary of the vibrational frequency results is presented in Table S1.

Table S1. Experimentally determined and harmonic and anharmonic vibrational frequencies calculated with DFT 0→1 vibrational frequencies (ω_{01}).

Molecule	Zero-field $\omega_{0\to1}$ (cm^{-1})	Harmonic $\omega_{0\to1}$ (cm^{-1})	Anharmonic $\omega_{0\to1}$ (cm^{-1})	Percent error (%)
Phenyl selenocyanate	2163.5	2271.8	2237.75	3.4
Benzonitrile	2234.6	2345.8	2311.0	3.4

2. Line shapes of phenyl selenocyanate in all solvents

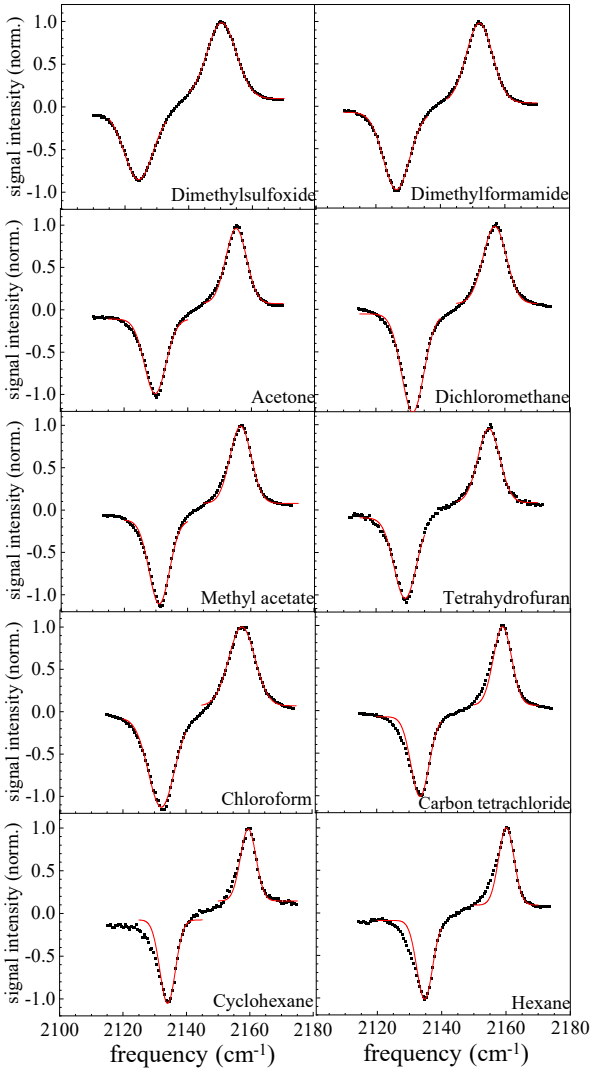

Figure S2. Pump-probe signal of the CN stretching vibration of PhSeCN in a series of non-aromatic and non-hydrogen bonding solvents. Gaussian fits to the 0→1 and 1→2 transition line shapes are shown as solid red lines. A summary of the parameters that describe the line shapes for PhSeCN is presented in Table S2.

Table S2. Line shape parameters for the 0⟶1 and 1⟶2 vibrational transitions of PhSeCN in a series of non-aromatic and non-hydrogen bonding solvents.

Solvent	ω_{01} (cm^{-1})	$\Delta\omega_{01}$ (cm^{-1})	ω_{12} (cm^{-1})	$\Delta\omega_{12}$ (cm^{-1})
Dimethyl sulfoxide	2150.3 ± 0.02	10.9 ± 0.05	2124.2 ± 0.06	10.6 ± 0.2
Dimethylformamide	2152.1 ± 0.02	9.6 ± 0.1	2126.4 ± 0.02	9.5 ± 0.1
Acetone	2155.2 ± 0.05	3.3 ± 0.06	2129.7 ± 0.05	8.0 ± 0.1
Dichloromethane	2156.9 ± 0.04	8.5 ± 0.1	2131.4 ± 0.05	8.1 ± 0.2
Tetrahydrofuran	2154.8 ± 0.04	8.0 ± 0.1	2129.0 ± 0.06	8.1 ± 0.2
Methyl acetate	2156.8 ± 0.03	7.9 ± 0.1	2131.0 ± 0.06	7.6 ± 0.2
Chloroform	2157.7 ± 0.03	4.1 ± 0.04	2132.2 ± 0.05	9.7 ± 0.1
Carbon tetrachloride	2158.9 ± 0.06	6.7 ± 0.1	2133.4 ± 0.04	6.6 ± 0.2
Cyclohexane	2159.5 ± 0.05	5.8 ± 0.1	2134.1 ± 0.04	5.8 ± 0.2
Hexane	2160.1 ± 0.03	5.7 ± 0.1	2134.7 ± 0.03	5.7 ± 0.1

3. Line shapes of benzonitrile in all solvents

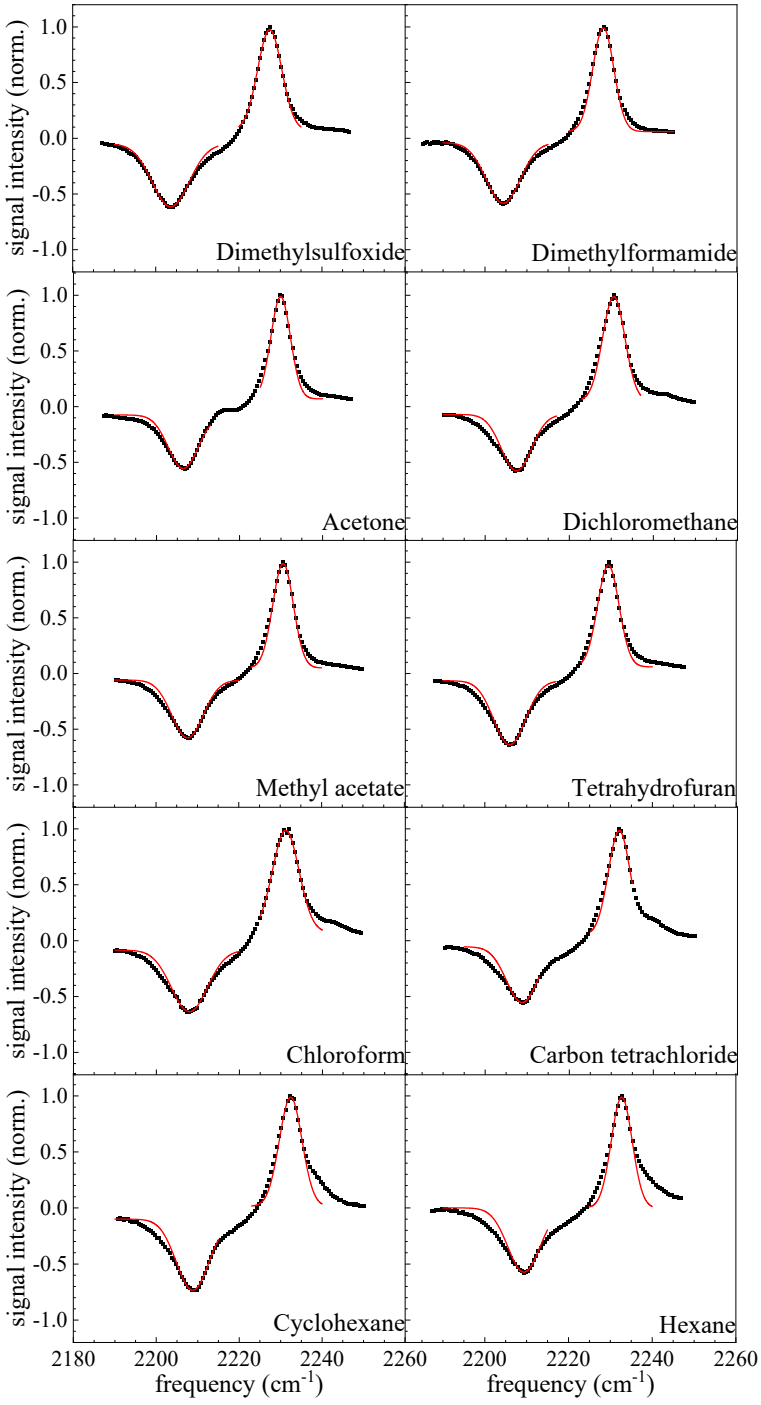

Figure S3. Pump-probe signal of the CN stretching vibration of BZN in a series of non-aromatic and non-hydrogen bonding solvents. Gaussian fits to the 0⟶1 and 1⟶2 transition line shapes are shown as solid red lines. A summary of the parameters that describe the line shapes for BZN is presented in Table S3.

Table S3. Line shape parameters for the 0⟶1 and 1⟶2 vibrational transitions of BZN in a series of non-aromatic and non-hydrogen bonding solvents.

Solvent	ω_{01} (cm^{-1})	$\Delta\omega_{01}$ (cm^{-1})	ω_{12} (cm^{-1})	$\Delta\omega_{12}$ (cm^{-1})
Dimethyl sulfoxide	2227.4 ± 0.03	6.8 ± 0.1	2203.6 ± 0.02	10.5 ± 0.1
Dimethylformamide	2228.2 ± 0.03	5.9 ± 0.1	2204.3 ± 0.02	9.6 ± 0.1
Acetone	2229.9 ± 0.03	5.5 ± 0.1	2206.4 ± 0.03	8.5 ± 0.1
Dichloromethane	2230.6 ± 0.02	6.3 ± 0.1	2207.4 ± 0.03	8.4 ± 0.1
Tetrahydrofuran	2229.5 ± 0.05	6.0 ± 0.1	2205.9 ± 0.02	8.9 ± 0.1
Methyl acetate	2230.7 ± 0.02	5.9 ± 0.1	2207.6 ± 0.02	9.0 ± 0.1
Chloroform	2231.2 ± 0.04	7.5 ± 0.1	2207.9 ± 0.04	10.2 ± 0.2
Carbon tetrachloride	2231.9 ± 0.03	6.1 ± 0.1	2208.8 ± 0.04	8.7 ± 0.1
Cyclohexane	2232.4 ± 0.04	6.4 ± 0.2	2208.8 ± 0.03	9.3 ± 0.1
Hexane	2232.7 ± 0.02	6.9 ± 0.1	2209.4 ± 0.02	3.0 ± 0.1

4. Line shape decomposition

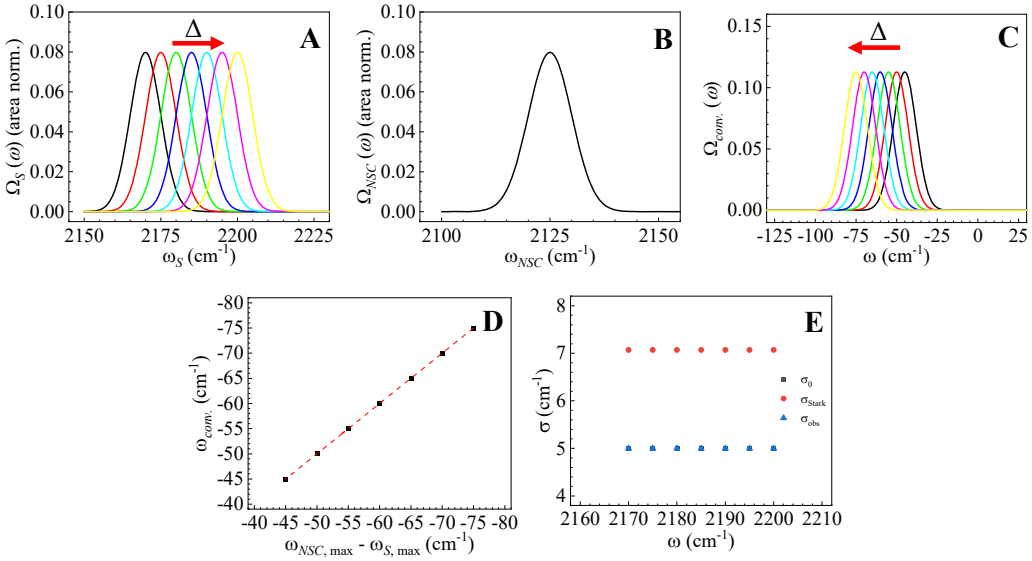

Figure S4. (A) Field dependent $\Omega_S(\omega)$, (B) solvent independent $\Omega_{NSC}(\omega)$, and (C) resulting $\Omega_{conv.}(\omega)$ spectra to observe the effect of the Stark contribution vibrational frequency shift on the NSC contribution. (D) The frequency of $\Omega_{NSC}(\omega)$ decreases linearly by $\Omega_S(\omega)$, and the resulting center frequency of the observed spectrum is located at the value $\omega_{NSC} - \omega_S$. (E) As expected, the resulting standard deviation is larger compared to the two individual contributions, but it remains fixed and it is not affected by the frequency shift of $\Omega_S(\omega)$.

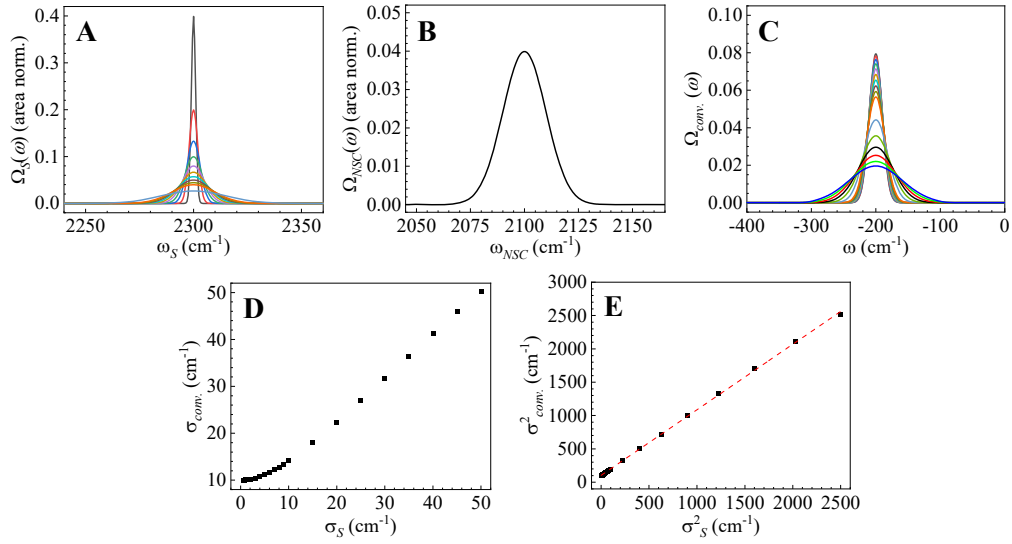

Figure S5. (A) Electric field-dependent standard deviation $\Omega_S(\omega)$, (B) solvent independent $\Omega_{NSC}(\omega)$, and (C) resulting $\Omega_{conv.}(\omega)$ to observe the effect of the Stark standard deviation on the observed final standard deviation. The square of the resulting standard deviation grows linearly with the square of the varying line shape width (E). In the limit that the Stark standard deviation is much smaller than the NSC standard deviation, only the latter is visible. In the reverse case, only the Stark standard deviation is visible (D).

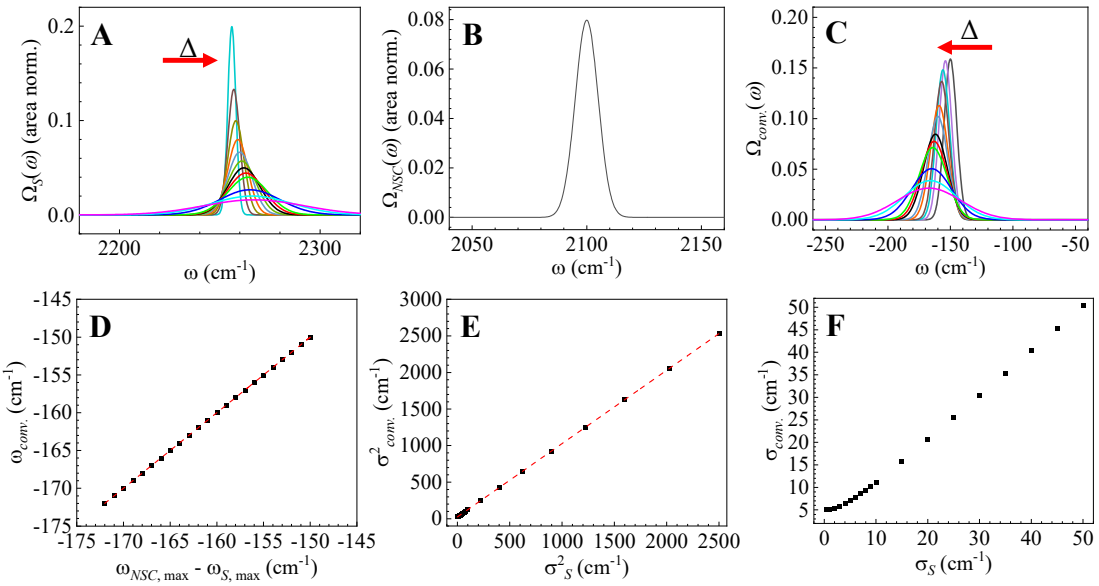

Figure S6. (A) Field dependent $\Omega_S(\omega)$ with moving center and increasing stadard deviation, (B) solvent independent $\Omega_{NSC}(\omega)$, and (C) resulting $\Omega_{conv.}(\omega)$. The Stark contribution broadens as it shifts in frequency to observe the effect this has on the zero-field spectra. The resulting center frequency is equal to the difference between the two input line centers and it incerases linearly with the Stark frequency shifts. The square of the resulting standard deviation increases linearly with the square of the Stark contribution standard deviation. In the limit that the Stark spectrum is much narrower than the zero-field spectrum, the resulting spectrum only displays the line width of the zero-field contribution. Conversely, in the limit that the Stark contribution is much broader than the zero-field contribution, the resulting spectrum only displays the standrad deviation of the Stark spectrum.

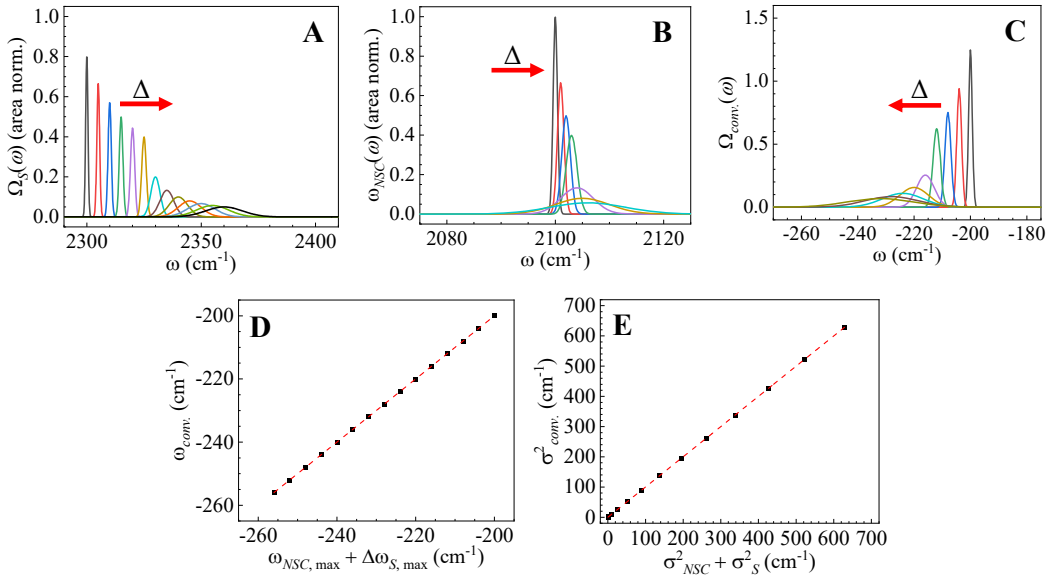

Figure S7. (A) Field dependent $\Omega_S(\omega)$, (B) solvent dependent $\Omega_{NSC}(\omega)$, and (C) resulting $\Omega_{conv.}(\omega)$ to observe the effect of varying the center frequency and width of both the Stark and NSC contributions on the final observed spectrum. The Stark and NSC contributions were allowed to shift in frequency and broaden at different rates. As expected, the center frequency of the resulting spectrum is equal to the difference between the two input spectra (D), whereas the square of the standard deviation increases linearly with the addition of the squares of the individual input spectra (E).

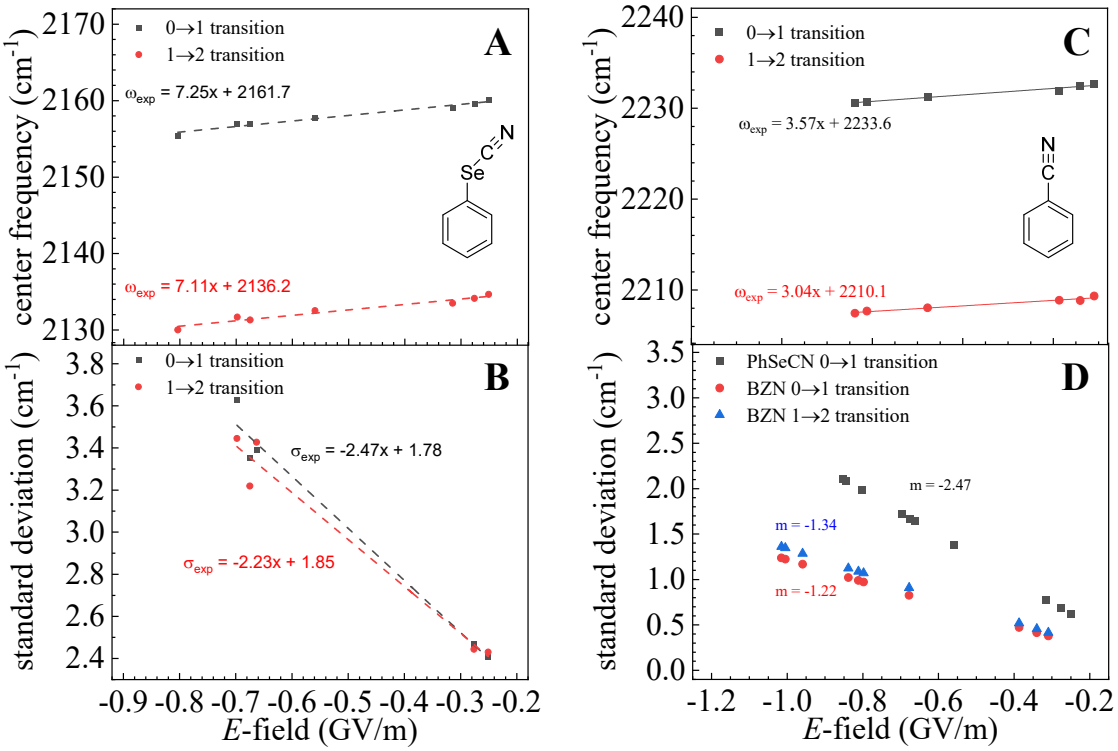

Figure S8. Linear fits to data subsets of (A) field dependent vibrational frequencies, (B) the spectral standard deviation of CN in PhSeCN's 0→1 and 1→2 transitions, and (C) the field-dependent CN vibrational frequencies in BZN's 0→1 and 1→2 transitions. Panel (D) shows the linear dependence of the spectral standard deviation of BZN's 0→1 transition (red) obtained approximately by reducing the slope of the equivalent data for PhSeCN (black) by the same percentage that BZN's vibrational frequency shift slope is smaller than in PhSeCN (49 %). The blue data in panel (D) corresponds to the linear dependence of the standard deviation in BZN's 1→2 transition obtained approximately by increasing the slope of its 0→1 by 10.5 %, which corresponds to the calculated percent increase in Stark tuning rate from second-order perturbation and density functional theories.

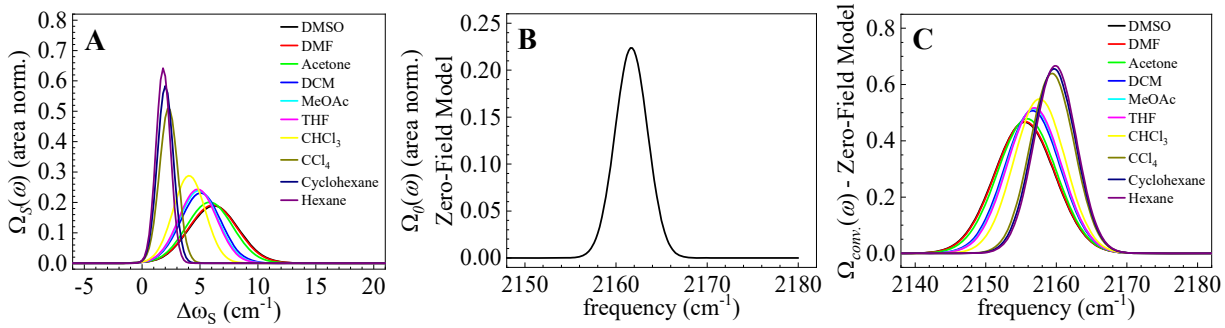

Figure S9. (A) Solvent dependent $\Omega_S(\omega)$, (B) solvent independent $\Omega_{NSC}(\omega)$, and (C) resulting $\Omega_{conv.}(\omega)$ of the zero-field model used to attempt a description of the experimental center frequency and standrad deviation data obtained from PhSeCN's 0→1 transition. The Stark contribution shifts and the standard deviation grows linearly with the solvent's field magnitude, whereas the zero-field spectrum is fixed. The resulting spectra shift in center frequency to lower values and broaden with the broadening Stark spectral width. It is shown in the main text that this set of spectra fail to reproduce the experimental data and demonstrate that the idea of a fixed zero-field contribution is not sufficient to explain the spectroscopic behavior of these vibrational probes.

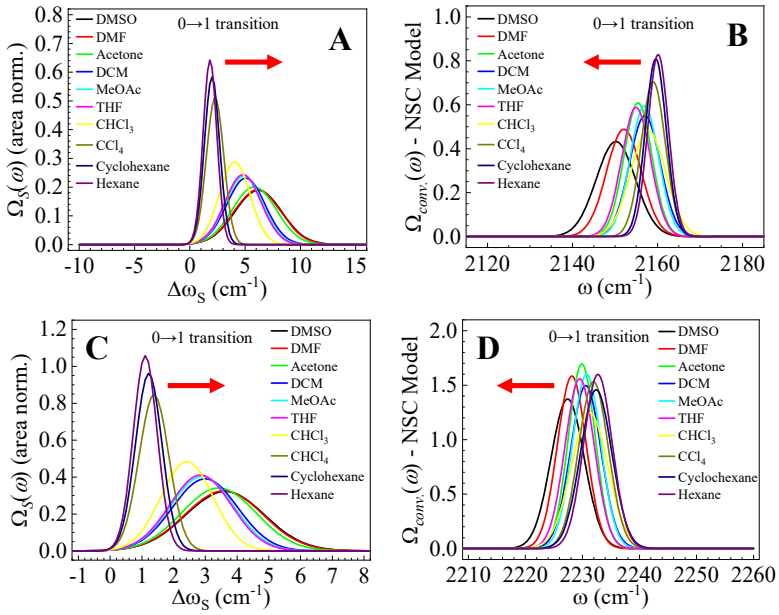

Figure S10. $\Omega_S(\omega)$ and $\Omega_{conv.}(\omega)$ spectral sets for the 0→1 transition of PhSeCN (A and B) and BZN (C and D) using the solvent dependent NSC model described in the main text. The red arrows show the direction in which the spectra shift as a function of the solvents' electric field. The Stark contribution broadens and shifts in frequency linearly with the magnitude of the solvents' electric fields. The convolution result reproduces the experimental data perfectly.

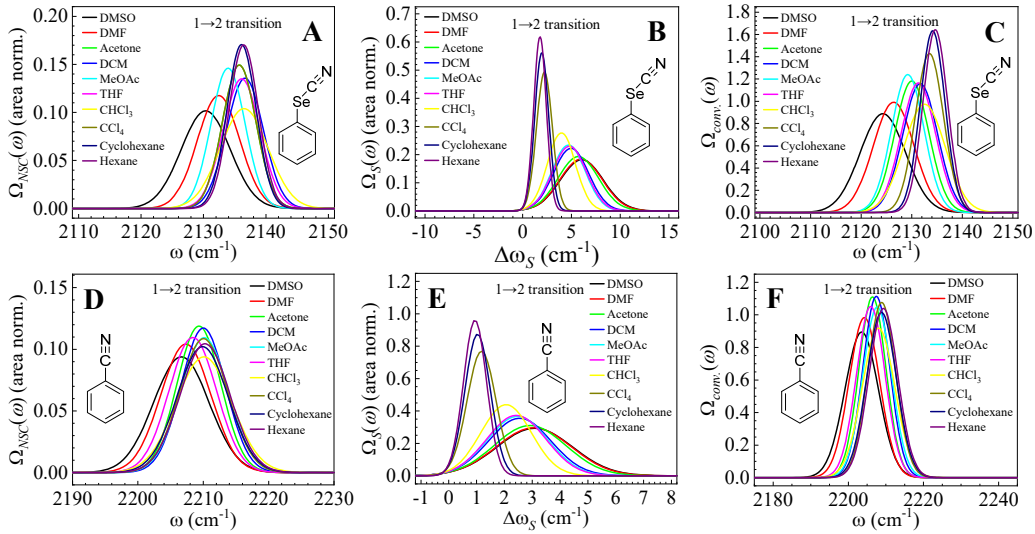

Figure S11. (A, D) Solvent dependent $\Omega_{NSC}(\omega)$, (B, E) Field dependent $\Omega_S(\omega)$, and (C, F) resulting $\Omega_{conv.}(\omega)$ used to model the experimental 1-2 transition data obtained from PhSeCN and BZN in the main text. The Stark contribution is taken to be linear in the electric field, and it broadens as it also shifts in frequency. The NSC contribution also shifts to take on solvent dependent center frequencies and line widths. However, these values do not change linearly. The net result is that the final spectra shift to lower frequency values with increasing solvent polarity. However, the change is not perfectly linear because the NSC contribution does not change linearly. The resulting spectra reproduce the experimental data obtained from the CN pump-probe line shapes in both PhSeCN and BZN. The NSC contribution is much broader in BZN than in PhSeCN. The physical origins of this difference is the subject of the main text of this manuscript and it is linked to the non-local nature of the CN stretching mode in BZN.

5. Linear absorption spectra

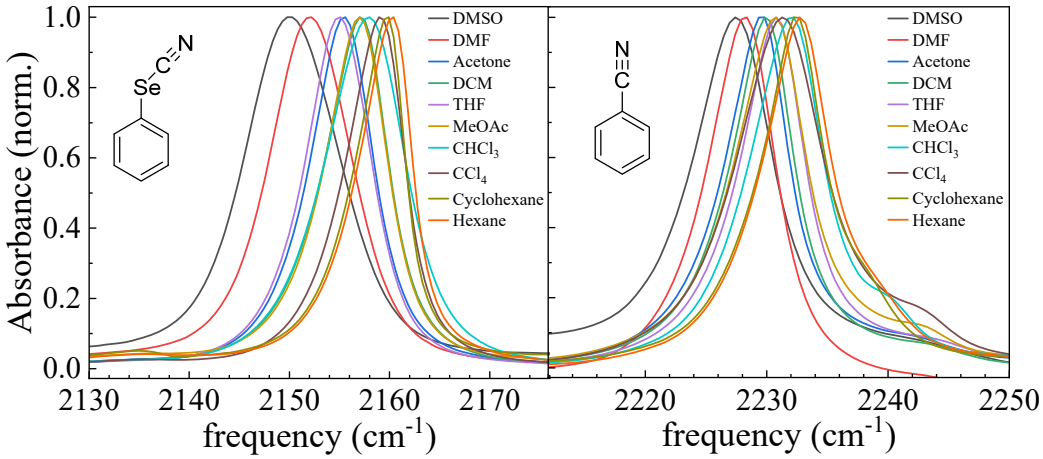

Figure S12. Linear absorption spectra of the CN stretch vibration in PhSeCN (left) and BZN (right) in a series of non-hydrogen bonding solvents. These spectra were used to confirm that the pump-probe transition line shapes are positioned at the correct vibrational transition values and to ensure that no signal contamination occurred in the PSPP experiment due to intramolecular vibrational relaxation of the CN stretching mode.

6. Cubic perturbation to harmonic oscillator

An anharmonic oscillator was modeled by adding a cubic perturbation, x^3, to the harmonic oscillator Hamiltonian as follows,

$$\begin{aligned} \underline{H} &= \underline{H}^0 + \underline{H}' \\ \underline{H}^0 &= \frac{1}{2}\hbar\omega_0(\underline{a}^-\underline{a}^+ + \underline{a}^+\underline{a}^-) \\ \underline{H}' &= q\underline{x}^3 \end{aligned} \tag{1}$$

Where $\underline{H}^0$ and $\underline{H}'$ are the unperturbed and perturbed Hamiltonians, respectively; $\hbar$ is the reduced Planck constant, ω_0 is the fundamental vibrational frequency of the mode, q is the amplitude of the cubic component, and $\underline{x}$ is the position quantum operator given by:

$$\underline{x} = \sqrt{\frac{\hbar\omega}{2k}}(\underline{a}^- + \underline{a}^+)\,. \tag{2}$$

where $\underline{a}^-$ and $\underline{a}^+$ are the raising and lowering quantum mechanical operators, and k is the harmonic spring constant. The cubic perturbation was applied to second order on the energies and the eigenkets using the following expressions:

$$E = E^0 + H'_{nn} + \sum_m{}' \frac{H'_{nm}H'_{mn}}{E_n^0 - E_m^0} \tag{3}$$

$$\left|\psi'_n\right\rangle = \left|\psi_n^0\right\rangle + \sum_j{}' \frac{H'_{jn}}{(E_n^0 - E_j^0)}\left|\psi_j^0\right\rangle + \sum_k{}' \left[\sum_m{}' \frac{H'_{km}H'_{mn}}{(E_n^0 - E_k^0)(E_n^0 - E_m^0)} - \frac{H'_{nn}H'_{kn}}{(E_n^0 - E_k^0)}\right]\left|\psi_m^0\right\rangle \tag{4}$$

where E^0 is the unperturbed energy of a harmonic oscillator state, ψ'_n is the perturbed vibrational energy state of interest, ψ_j^0 and ψ_m^0 are vibrational states coupled by the cubic perturbation to the unperturbed vibrational state, ψ_n^0 ; the prime superscript on the summation means it is performed over indices of m and j that are different from n, and H'_{nm} is the first-order perturbation given by its expectation value $\left\langle m\left|q\underline{x}^3\right|n\right\rangle$. To second order, the corrected energies and normalized eigenkets are given by

$$E_n = \left[n + \frac{1}{2}\right]\hbar\sqrt{\frac{k}{\mu_m}} - \left[30n^2 + 30n + 11\right]\left(\frac{q\hbar}{k\sqrt{\mu_m}}\right)^2 \tag{5}$$

$$\left|\psi'_n\right\rangle = \frac{1}{\sqrt{1 + \sum_{i=0}^{4} q^2 C_i^* C_i}}\left(\begin{array}{l}\left|\psi_n^0\right\rangle + q^2C_5\left|\psi_{n-6}^0\right\rangle + q^2C_6\left|\psi_4^0\right\rangle + qC_1\left|\psi_{n-3}^0\right\rangle + q^2C_7\left|\psi_{n-2}^0\right\rangle + qC_2\left|\psi_{n-1}^0\right\rangle + \\ qC_3\left|\psi_{n+1}^0\right\rangle + q^2C_8\left|\psi_{n+2}^0\right\rangle + qC_4\left|\psi_{n+3}^0\right\rangle + q^2C_9\left|\psi_{n+4}^0\right\rangle + q^2C_{10}\left|\psi_{n+6}^0\right\rangle\end{array}\right) \tag{6}$$

sespectively, where C_i are the coupling coefficients between state n and other vibrational states. The normalized harmonic wave functions, used in Eq. 6 are given by:

$$\left|\psi^{0}{}_{n}\right\rangle = \left[\left(\frac{\alpha}{\pi}\right)^{\frac{1}{2}} \frac{1}{2^n n!}\right]^{\frac{1}{2}} e^{\frac{-\alpha}{2}x^2} H_n(x) \tag{7}$$

$$\alpha = \frac{\mu_m}{\hbar}\sqrt{\frac{k}{\mu_m}} \tag{8}$$

Where μ_m is the reduced mass of the molecular probe (i.e., approximated as the reduced mass of the CN group), and $H_n(x)$ is the Hermite polynomials. The algebraic expressions for all coupling coefficients can be found in Table S4. Eq. 5 is used to determine expressions for the 0→1 and 1→2 vibrational transition frequencies, $\omega_{n\to m}$, of the CN stretching vibration, as well as for the molecular anharmonicity, $\Delta\omega$, as follows,

$$\omega_{n\to m} = E_m - E_n$$

$$\Delta\omega = \omega_{n\to m} - \omega_{m\to m+1} \tag{9}$$

Values of k and q are needed to generate the anharmonic wave functions given by Eq. 6. These values were chosen such that they reproduce the experimentally determined zero-field vibrational frequency values of the 0→1 and 1→2 vibrational transition frequencies, and their anharmonicity (Eq. 9). The zero-field frequencies (obtained from a linear fit to the field dependent frequency data) were used because they most accurately correlate with the *in-vacuo* DFT calculations. The values of k and q are presented in Table 1 of the main text. Once k and q are known, Eqs. S6-S8 are used to determine analytical expressions for the wave functions of states $\left|0\right\rangle$, $\left|1\right\rangle$, and $\left|2\right\rangle$. The resulting wave function probability amplitudes are shown in Fig. 10 of the main text. Finally, k and q were used to plot an anharmonic potential for the CN mode of PhSeCN and BZN using the following expression:

$$v(x) = \frac{1}{2}kx^2 - qx^3 \tag{10}$$

Table S4. Coupling coefficients of wave function obtained from second-order non-degenerate perturbation theory.

Coefficient	Expression
C_1	$\sqrt{n^3 - 3n^2 + 2n}$
C_2	$9n\sqrt{n}$
C_3	$9(n+1)$
C_4	$\sqrt{n^3 + 6n^2 + 11n + 6}$
C_5	$\frac{1}{18}\sqrt{\prod_{i=0}^{5}(n-i)}$
C_6	$\left(n - \frac{3}{4}\right)\sqrt{\prod_{i=0}^{3}(n-i)}$
C_7	$\left(\frac{7}{2}n^2 - \frac{19}{2}n + \frac{1}{2}\right)\sqrt{\prod_{i=0}^{1}(n-i)}$
C_8	$\left(\frac{7}{2}n^2 - \frac{33}{22}n + \frac{27}{2}\right)\sqrt{\prod_{i=1}^{2}(n+i)}$
C_9	$\left(n + \frac{7}{4}\right)\sqrt{\prod_{i=1}^{4}(n+i)}$
C_{10}	$\frac{1}{18}\sqrt{\prod_{i=1}^{6}(n+i)}$

In parallel, DFT was used to obtain the potential energy surface of the CN stretching normal mode for PhSeCN and BZN as a function of normal mode displacement (see experimental

section). The two potential energy surfaces are shown in Fig. 10, and the vertical position of each wave function probability is determined with Eq. S7.

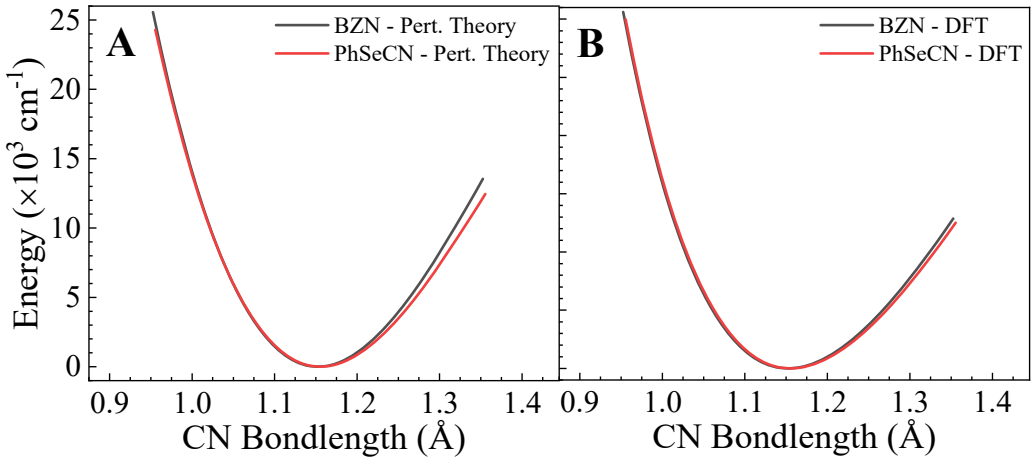

Figure S13. A comparison of the PES of the CN stretching mode in PhSeCN and BZN obtained from (A) perturbation theory and (B) DFT shows that the CN stretching mode in PhSeCN is more anharmonic than in BZN. These calculations agree with experimental measurements of the anharmonicity (see Fig. 2).

Fig. 10 shows that DFT and perturbation theory yield quantitatively equivalent potential energy surfaces up to the energy of the second excited state, and demonstrate that it is appropriate to combine the two types of calculations to perform the desired dipole projection weighting calculations (see below). The probability of the wave function at each energy level extends out farther for PhSeCN compared to BZN, owing to its more anharmonic potential.

Using DFT, the molecular dipole moments of both BZN and PhSeCN were calculated as a function of normal mode displacement. The vector coordinates of the molecular dipole moment, and the CN atoms were then used to compute the projection of the dipole moment along the CN bond axis. The goal of this calculation was to obtain the percent difference of the dipole projection vector for the 0→1 and 1→2 vibrational transitions of each molecule. The molecular dipole and molecular dipole projection onto the CN bond axis are shown in Fig. S14.

To determine a single value for the dipole and its projection, the contribution of each dipole value along the normal mode was weighted using the wave function probability of each state given by $\left|\psi_n'(x)\right|^2$. The wave function probability weighted molecular dipole and molecular dipole projection were calculated using the following expression,

$$\left\langle proj_{\overline{\mathrm{CN}}}\vec{\mu}_n \right\rangle = \int_{-\infty}^{\infty} \sum_{i=1}^{N} a_i x^i \left|\psi_n'(x)\right|^2 dx \tag{11}$$

where x is the normal mode displacement axis, n is the vibrational energy level index, $\left\langle proj_{\overline{\mathrm{CN}}}\vec{\mu}_n \right\rangle$ is the weighted average value of the molecular dipole moment projection onto the CN bond axis for energy level n, a_i are the coefficients of the polynomial fit to the dipole and dipole projection curves, and $\left|\psi_n'(x)\right|^2$ is the second-order normalized perturbed wave function probability for energy level n. In the specific case of PhSeCN and BZN, the dipole and dipole projection curves are both best described by a second order polynomial fit, with $N = 2$, but that need not be the case for other chemical structures or vibrational modes. The resulting weight averaged dipole and dipole projections are shown in Table 4.

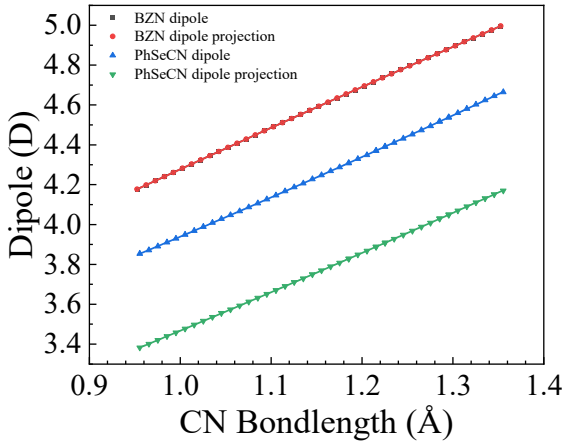

Figure S14. Permanent dipole moment and permanent dipole moment projection onto the CN bond axis of both PhSeCN and BZN as a function of CN bond length. In BZN, the permanent dipole moment vector is collinear with the CN bond axis, so the dipole moment and the dipole moment projection are equal. In PhSeCN, because the two vectors are not collinear, the magnitude of the dipole projection by 11 %.

7. Mulliken charge analysis

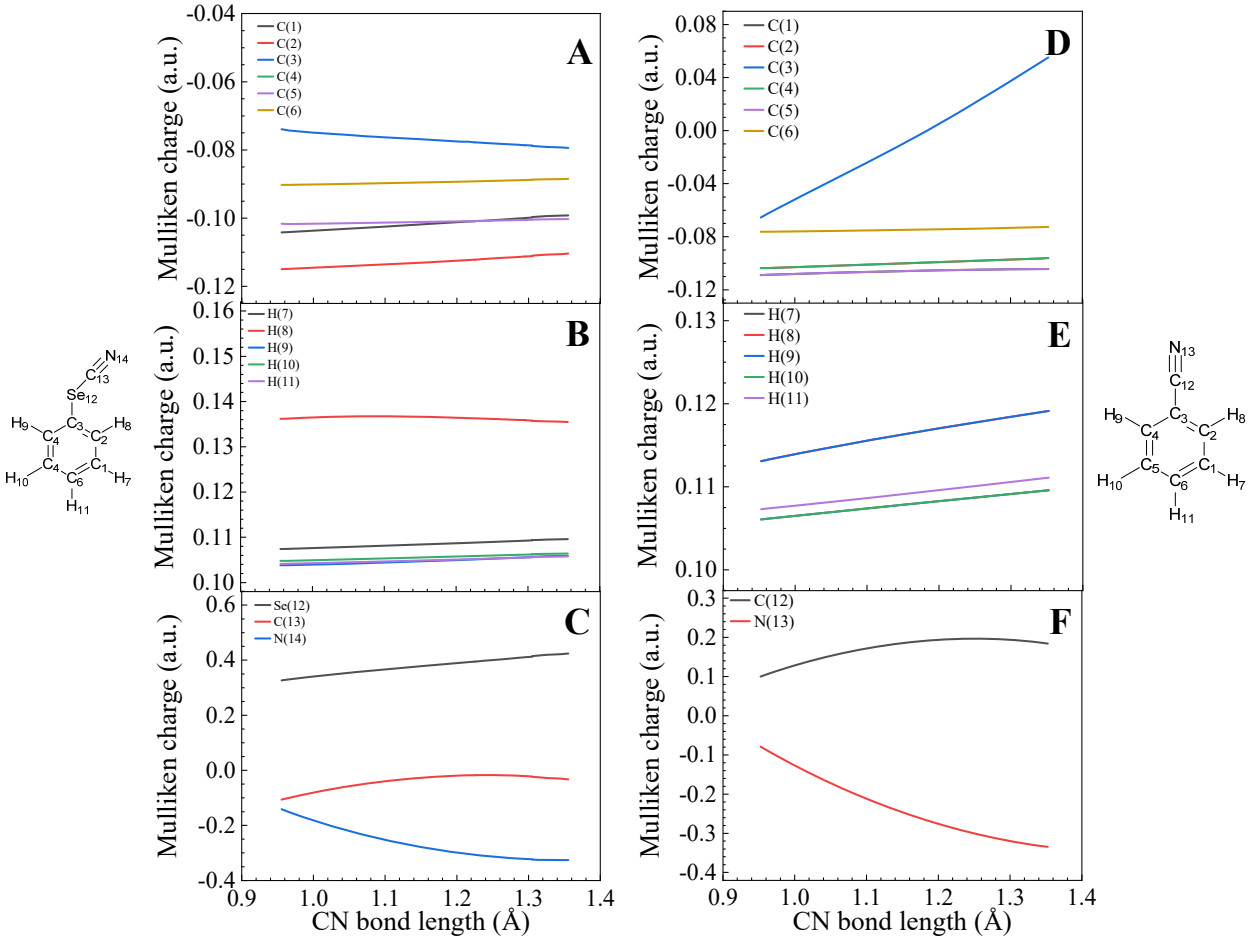

Figure S15. Mulliken atomic charges of carbons (A and D), hydrogens (B and E) and non-phenyl ring atoms (C and F) for both PhSeCN (left) and BZN (right). The *ipso* carbon was chosen to illustrate the differences in charge separation that result from excitation of the CN mode in both molecules. The charge on this carbon changes dramatically in BZN, while it remains constant in PhSeCN. This indicates that the phenyl ring in BZN is involved in the CN stretch normal mode vibration. By contrast in PhSeCN, the heavy Se atom decouples the CN vibration from the rest of the molecule and prevents the phenyl ring from being involved in this vibration, thus making the CN stretch more of a local mode compared to BZN's. We identify this difference between the two molecules as the reason for the larger magnitude of the NSC component and for the greater increase in Stark tuning rate of the 1→2 transition over the 0→1 transition in BZN compared to PhSeCN. The greater charge separation that occurs in BZN upon CN excitation results in a larger permanent dipole moment for BZN. The non-local nature of the CN stretch in BZN also allows for the intermolecular interactions that result in the NSC component to the linewidth and center frequencies to be stronger because they indirectly involve the phenyl ring and increase inhomogeneous line broadening. In PhSeCN, since the CN mode is a local mode, and only interactions directly between the solvent and the CN stretch result in inhomogeneous broadening, thus decreasing the magnitude of the NSC component in the experimental data.

8. Examples of other molecules with similar behaviors.

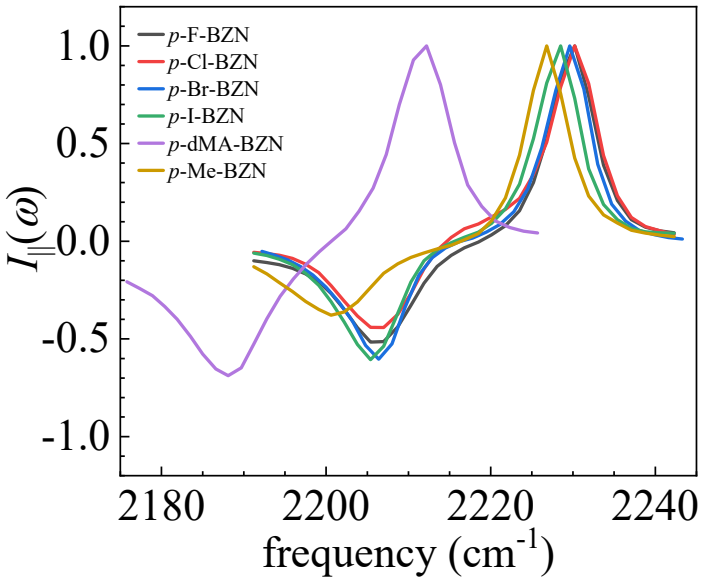

Figure S16. Pump-probe spectra of the CN stretching vibration of a series of *p*-substituted benzonitrile structures. All show the same types of differences in linewidths between the 0→1 and 1→2 transitions as BZN.

9. Vibrational transition dependent Stark tuning rate

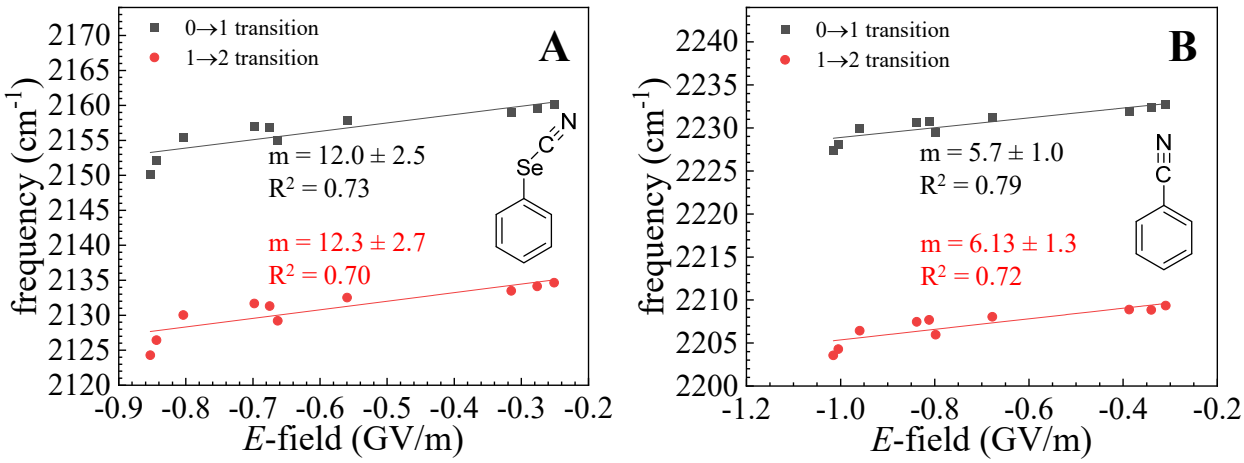

Figure S17. Linear regression fits to the vibrational transition center frequency of the 0→1 and 1→2 transitions for (A) PhSeCN and (B) BZN. The slope and R^2 values of all fits are shown next to the corresponding data sets. It is clear that while the data displays a linear trend in the low field regime, there is a significant departure from linearity in the high field regime.